NANO LETTERS

2004
Vol. 4, No. 5
963−968

Crystalline Boron Nanoribbons: Synthesis and Characterization

Terry T. Xu,[†] Jian-Guo Zheng,[‡] Nianqiang Wu,[‡] Alan W. Nicholls,[§] John R. Roth,[§] Dmitriy A. Dikin,[†] and Rodney S. Ruoff*[,†]

Department of Mechanical Engineering, Northwestern University, Evanston, Illinois 60208, NUANCE Center, Northwestern University, Evanston, Illinois 60208, and Research Resource Center, University of Illinois at Chicago, Chicago, Illinois 60612

Received January 20, 2004; Revised Manuscript Received March 3, 2004

ABSTRACT

Catalyst-free growth of boron nanoribbons was observed by pyrolysis of diborane at 630–750 °C and ~200 mTorr in a quartz tube furnace. Nanodiffraction analysis indicates the nanoribbons are single crystal α-tetragonal boron. TEM images show the nanoribbon is covered by a 1–2 nm thick amorphous layer. Elemental analysis by EELS, EDX, and XPS shows the nanoribbons consist of boron with small amounts of oxygen and carbon. Infrared and Raman spectra are also reported.

Boron is a unique element with structural complexity due to its electron-deficient nature.[1−3] Extensive fundamental and applied research of bulk boron and boron-rich materials has been reported, for example, in refs 1 and 2. Boron allotropes as well as many boron-rich materials have B_{12} icosahedra. Boron has a high melting point (~2200 °C), low density (2.340 g/cm^3), moderate oxidation resistance, high hardness (Knoop: 2160−2900), high Young's modulus (380−400 GPa),[4,5] and interesting optical and electrical properties.[1] The application of boron includes high-temperature devices, nuclear engineering, high-energy fuel, coatings, and others.[1]

More recently, the atomic structure and electronic states of boron-based nanostructures have been theoretically studied.[6−11] Based on an Aufbau principle[6] by Boustani, novel layered,[8,10] tubular,[9,10] and quasi-crystalline boron solids[7,10] built from elemental subunits are predicted to be relatively stable. Single-shell boron nanotubes are predicted to have high metallic conductivities irrespective of whether they have zigzag, armchair, or chiral structure.[9,10] Single-shell AlB_2 nanotubes are also predicted to be metallic.[11] These new boron-based nanomaterials, if synthesized, may have potential applications in nanoelectronics, in high-temperature electron devices, and in nanocomposites where they may impart stiffness, toughness, and strength.[10]

There have been several recent papers on the synthesis of boron nanostructures.[12−21] Amorphous boron nanowires (B NWs) were synthesized by a chemical vapor transport method using boron and iodine as precursor,[12,13] and also by laser ablation of a B target.[14] Well-aligned amorphous B NWs and feather-like B NWs were fabricated by magnetron sputtering of high purity B/B_2O_3 or B targets.[15,16] Crystalline boron nanowires have been synthesized by laser ablation of a B/NiCo target,[17] chemical vapor deposition (CVD) using diborane (B_2H_6) as precursor and NiB as catalyst,[18] post-annealing of amorphous B NWs at high temperature (1050 °C),[19] and pyrolysis of B_2H_6 in the nanopores of a porous alumina template at 800 °C.[20] Recently, crystalline boron nanobelts were synthesized by laser ablation of high-purity boron pellets at 700−1000 °C.[21]

In this letter, the catalyst-free growth of single-crystal α-tetragonal boron nanoribbons by pyrolysis of diborane at relatively low temperature (630−750 °C) and low pressure (200 mTorr) is reported. In 1990, Komatsu et al.[22] reported the growth of boron whiskers and ribbons in a low-pressure plasma mixture of B_2H_6, He, and H_2. Their[22] synthesis temperature (880 °C) and pressure (~1500 mTorr) was higher than ours. The synthesized ribbons have similar morphology as those we report, but were assigned as the rhombohedral structure[22] rather than the α-tetragonal structure.

Our experiments were carried out in a home-built furnace system. A schematic is shown in Figure 1. The reaction chamber is a quartz tube (25 mm o.d., 22 mm i.d., 16 in. length; Quartz Scientific) located between two semicylindrical ceramic fiber heaters (6 in. long heating zone; Watlow). The gas flow rates were monitored by mass flow controllers (810 series, Sierra Instruments), and the pressure measured by a convection gauge (Kurt J. Lesker). A liquid nitrogen-cooled trap (Kurt J. Lesker) is used to trap condensable vapors and volatiles before they enter the mechanical pump. It also traps oil vapors that otherwise might enter the

* Corresponding author. Telephone: (847) 467-6596. Fax: (847) 491-3915. E-mail: r-ruoff@northwestern.edu.
[†] Department of Mechanical Engineering, Northwestern University.
[‡] NUANCE Center, Northwestern University.
[§] Research Resource Center, University of Illinois at Chicago.

10.1021/nl0498785 CCC: $27.50
Published on Web 04/01/2004

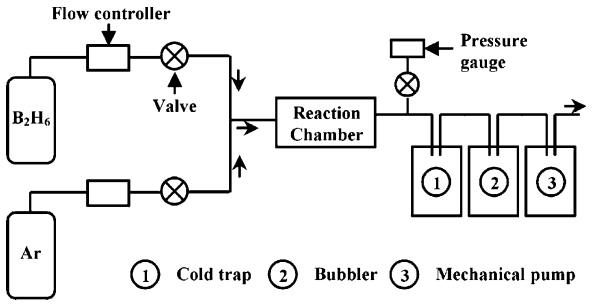

Figure 1. Schematic of the CVD system for growth of boron nanostructures.

reaction chamber from the mechanical pump. The system can be operated in the temperature range from room temperature to 1050 °C, and in the pressure range from a few millitorr to several atm.

Silicon (Si) substrates with one-micron thick thermally grown SiO_2 (1×1 cm^2, University Wafer) were used for the experiments. They were ultrasonically cleaned using acetone and ethanol (Crest ultrasonic cleaner; 5 min), followed by oxygen plasma cleaning (Plasma-862, Kurt J. Lesker; 3 min). The Si substrates were then loaded in a quartz boat and placed in the reaction chamber. The chamber was ramped up to 900 °C (center position temperature) in 60 min with 15 sccm (standard cubic centimeter) continuous flow of argon (BOC gases). A gas mixture of 15 sccm diborane (5% in argon, Voltaix) and 15 sccm argon was then introduced into the chamber for 45 min. The total pressure for each run was ~200 mTorr (for any particular run the pressure was known to 3 significant figures). After reaction, several dark gray "puffy balls" (visible to the eye) were found randomly deposited on the substrates, but only if they were positioned in the 1-cm long 630−750 °C temperature zone region in our furnace system. These substrates were removed, and the puffy ball deposits were characterized by scanning electron microscopy (SEM), transmission electron microscopy (TEM) including electron energy loss spectroscopy (EELS) and energy-dispersive X-ray spectroscopy (EDX), X-ray photoelectron spectroscopy (XPS), Fourier transform infrared spectrometry (FTIR), and Raman spectroscopy.

Figures 2a−d are a series of SEM micrographs recorded using a LEO 1525 FE-SEM. Figure 2a shows a typical puffy ball. The ball diameter is ~230 μm. A closer view reveals that the puffy ball consists of nanostructures with different morphologies. Figure 2b shows several partially scrolled nanostructures. The width of these "nanoscrolls" (calculated as if they could be unrolled) varies from 800 to 3200 nm, and the thickness is in the range of 15−20 nm. The inset in Figure 2b shows the cross-section of one ~17 nm thick scroll. Figure 2c shows the "grass-like" nanoribbons. These nanoribbons are 200 nm to 500 nm wide, thus smaller than the hypothetically unrolled scrolls. The nanoribbons, like the "nanoscrolls" shown in Figure 2b, are ~20 nm thick. The "grass-like" nanoribbons have three distinct features, as shown in the insets of Figure 2c: (i) they are typically twisted; (ii) not all have straight edges, some edges are zigzag; (iii) the tips (or ends) of some nanoribbons have slots in the middle, forming a "fork-like" structure. Figure 2d shows a "palm leaf-like" nanostructure, in which the ends of nanoribbons split into several nanowires. The inset shows

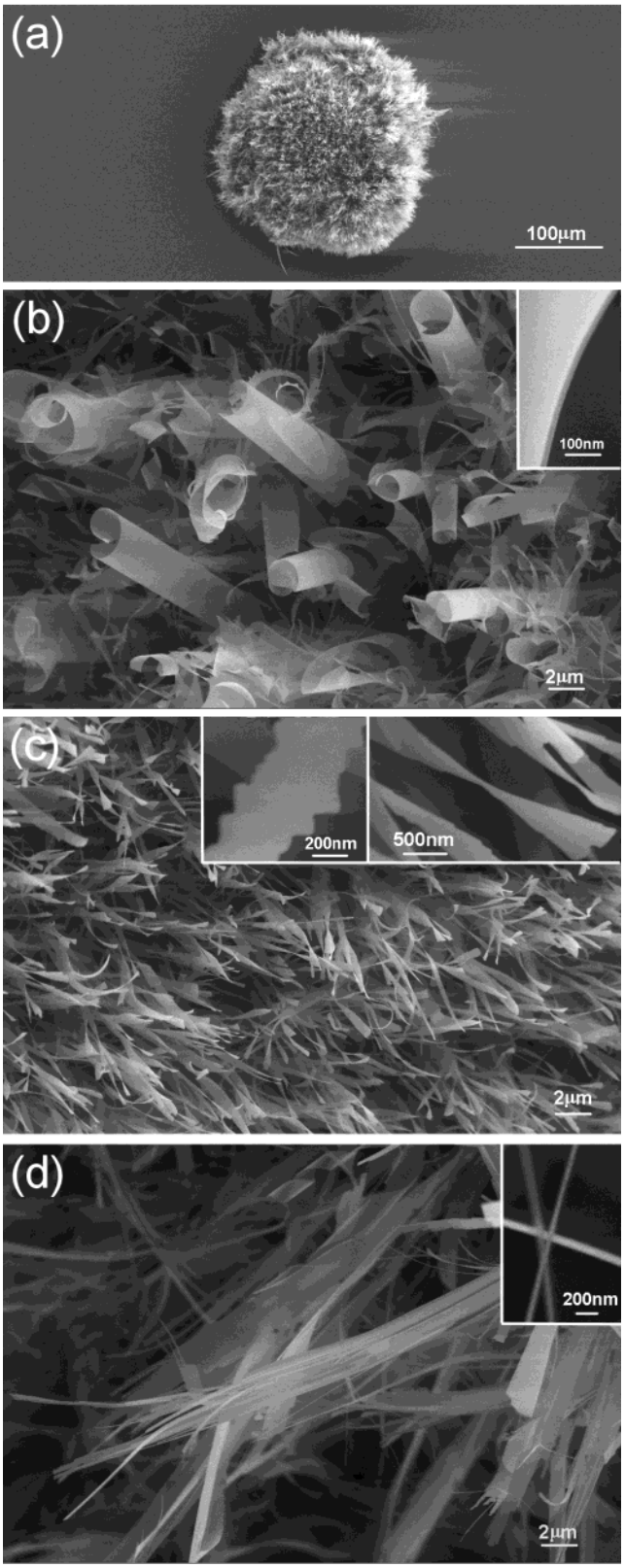

Figure 2. SEM micrographs. (a) Overall view of the puffy ball. (b) Scrolled nanostructures. The inset shows the cross-section of one "nano-scroll" of thickness 17(±2) nm. (c) "Grass-like" nanoribbons. The insets show that the nanoribbons are easily twisted and some have "zigzag" edges. (d) "Palm-leaf like" nanostructures. Nanoribbons have split ends, forming smaller nanostructures.

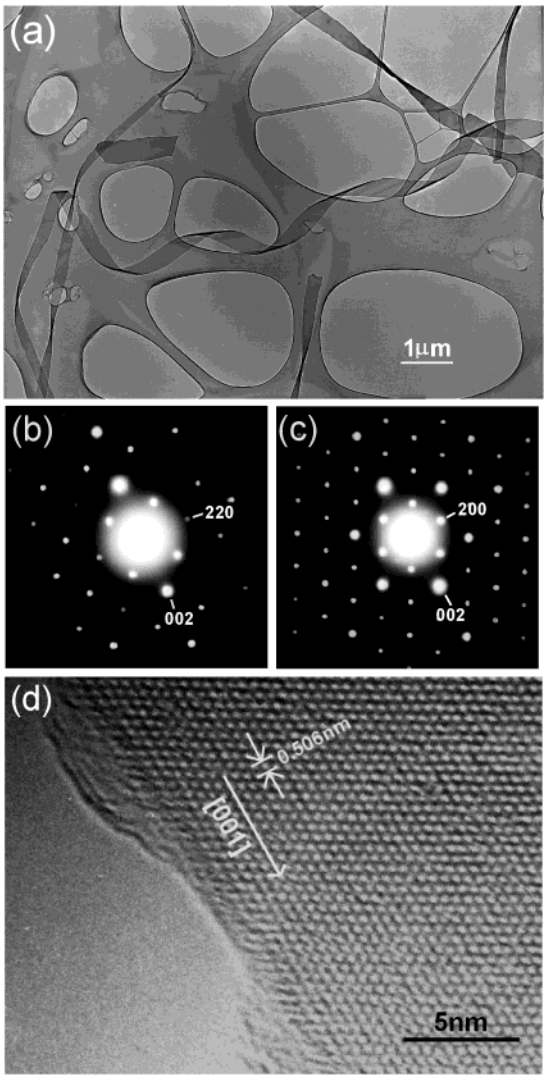

Figure 3. (a) TEM micrograph of several twisted nanoribbons at lower magnification. Diffraction patterns recorded along (b) the [$\bar{1}$10] zone axis, and (c) the [010] direction. (d) HR-TEM image of part of the nanoribbon, showing crystallized structure and the preferential growth along the [001] axis. Note thin amorphous layer, left side.

an enlarged image of three nanowires. The width of the nanowires varies from 20 to 100 nm. Among these three different morphologies of nanostructures, the "grass-like" nanostructure was most common.

Several puffy balls were scraped off the substrates and ultrasonically dispersed in ethanol (Crest ultrasonic cleaner, 60 min). A drop of suspension was placed on a copper TEM grid covered with a lacy carbon film (SPI Supplies). Morphology and crystal structure were investigated with a Hitachi H-8100 TEM. The camera length of the microscope was calibrated with a single-crystal silicon (100) sample. High-resolution TEM (HR-TEM) images were obtained with a Hitachi HF-2000 FE-TEM.

Figure 3a shows a TEM micrograph of several twisted nanoribbons. The width of these nanoribbons ranges from 200 to 400 nm, which is consistent with the results measured by SEM shown in Figure 2c. Electron diffraction was done on several nanoribbons to determine their structures. For each

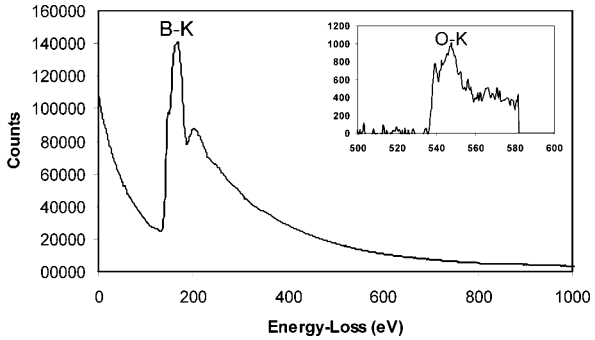

Figure 4. A representative EELS spectrum obtained from a boron nanoribbon, showing a high-intensity boron core-loss peak at ~188 eV and a weak oxygen core-loss peak at ~532 eV. The spectrum was recorded after the sample was exposed to air for 64 days.

nanoribbon, a series of nanodiffraction patterns were recorded by tilting the sample to different low-index zone axes. It was found that the nanoribbons are crystalline. The calculated lattice constants are $a = 0.879 \pm 0.009$ nm and $c = 0.509 \pm 0.005$ nm, which coincide closely with the values of α-tetragonal boron from the JCPDS database[23] (#75−0511: $a = 0.875$ nm, $c = 0.506$ nm; #75−0218: $a = 0.873$ nm, $c = 0.503$ nm). Figures 3b and 3c are two representative diffraction patterns recorded from one nanoribbon in the [$\bar{1}$10] and [010] axes, respectively. The measured angle between the two zone axes is 45°, which is in agreement with the angle expected for a tetragonal structure. Figure 3d is a representative HR-TEM image, showing the nanoribbon is crystallized and covered by a 1−2 nm thick amorphous layer. The preferential growth direction was determined to be the [001] direction.

The chemical composition of the nanoribbons was analyzed by EELS using a JEOL JEM 2010F TEM, and EDX using a JEOL JEM 3010 TEM. Our original EELS spectra detected only boron in the nanoribbons. No carbon or oxygen was detected. However, EDX analysis detected both boron and a small amount of oxygen. The slightly different results obtained by EELS and EDX are rationalized in terms of the different detection threshold for these two techniques.[24]

The same sample was reanalyzed by EELS after it was exposed to air for several months. In addition to the high-intensity boron core-loss peak, a very weak intensity oxygen core-loss peak was also detected. Figure 4 is a representative EELS spectrum recorded after the sample was exposed to air for 64 days. It shows the characteristic boron K-shell ionization edge at ~188 eV. Examination of the spectrum obtained after subtraction of the background indicated that there was a small peak corresponding to the oxygen K-shell ionization at ~532 eV (see inset). Quantitative analysis[25] showed the amount of the oxygen was about 4.3 ± 0.6 at. %.

Boron is superficially oxidized in air at room temperature.[1,2] To avoid this, it was suggested that boron needs to be stored under vacuum or in inert atmosphere.[1,2,26] Cooper reported[26] that boron powders (having a mixture of α-tetragonal and orthorhombic phases) 0.1−10 μm in particle size oxidized slowly at room temperature. The concentration of B changed from 99% to 92% after a few months' exposure

in a laboratory, due to the formation of an oxide layer.[26] In our experiment, considering the fact that the oxygen core-loss peak was more visible after the sample was exposed to air for more than two months, we believe the small amount of oxygen was most likely from the surface oxidation of the boron nanostructures.

To further analyze the chemical composition and the chemical structure of the nanoribbons, XPS analysis was performed. Several puffy balls were scraped off the substrate and pressed to a pellet. XPS analyses were performed on the pellet with an Omicron ESCA probe, which was equipped with an EA125 energy analyzer. Photoemission was stimulated by a monochromated Al Kα radiation (1486.6 eV) with an operating power of 300 W. The analyzer was operated in the constant analyzer energy (CAE) mode at 60 eV (survey scan) and 25 eV (detailed scan) of core level lines. Binding energies were referenced to the C 1s binding energy set at 285.0 eV.

Figure 5a shows the XPS survey-scan spectrum for binding energies from 0 to 1200 eV. In addition to the boron and oxygen peaks, a weak carbon peak was detected. Quantitative analysis revealed that the interrogation volume by XPS for the nanoribbons contained ~82.5 at. % boron, ~14.3 at. % oxygen, and ~3.2 at. % carbon. As discussed below in the text, the small amount of carbon probably is from both surface contamination and carbon in the interior of the boron nanoribbons. Since XPS is a surface analysis tool, it is not surprising that a higher apparent oxygen content, from an oxidized surface layer on the nanoribbons, is found as compared to EELS.

Figure 5b shows the B 1s core-level spectrum. Upon inspection of the peak shape, the B 1s spectrum was fit to four components. The main component at 187.5 eV corresponded to the B−B bond. The binding energy of 187.5 eV was in good agreement with the reported value obtained from bulk boron (187.3−187.9 eV).[27−29] It has also been reported that the formation of the B−C bonds can result in a shift of up to ~0.6 eV in the B 1s binding energy with respect to that of pure bulk boron.[27,29] Therefore, the component at 188.1 eV was assigned to B−C bonds. The higher binding energy components at 188.9 eV and 193.1 eV were due to the oxidation of boron. The component at 188.9 eV was assigned to the B−O bond in a boron-rich oxide in which an oxygen atom is coordinated with several boron atoms (B_x−O).[29,30] This B−O bond resulted in the presence of an O 1s feature at 533.0 eV in Figure 5d. The highest energy component of the B 1s spectrum, at 193.1 eV in Figure 5b, as well as the corresponding O 1s feature at 533.8 eV in Figure 5d were clearly characteristic of B_2O_3.[28,31] The formation of B_2O_3 is thermodynamically favored due to the larger bond energy compared to the competing bonds (808 kJ/mol for B−O, 448 kJ/mol for B−C, and 297 kJ/mol for B−B).[32] But the slow oxidation over a several month period suggests a kinetic barrier to oxidation at room temperature, such as are present for the oxides on silicon or aluminum.

Figure 5c shows the C 1s core-level spectrum. The C 1s peak was broad and asymmetric. It was fit to three components. The main component at 285 eV was assigned as being due to the C−C bond from hydrocarbon surface contamination. The low energy component at 284.2 eV was assigned as due to B−C bonding.[27,29] This C 1s spectrum component was associated with the B 1s component at 188.1 eV in Figure 5b. The C 1s component at 286.5 eV was assigned as due to either a C−O bond or C−OH bond.[33] A corresponding O 1s component associated with the C−O (or C−OH) bond appeared at 531.9 eV in Figure 5d.

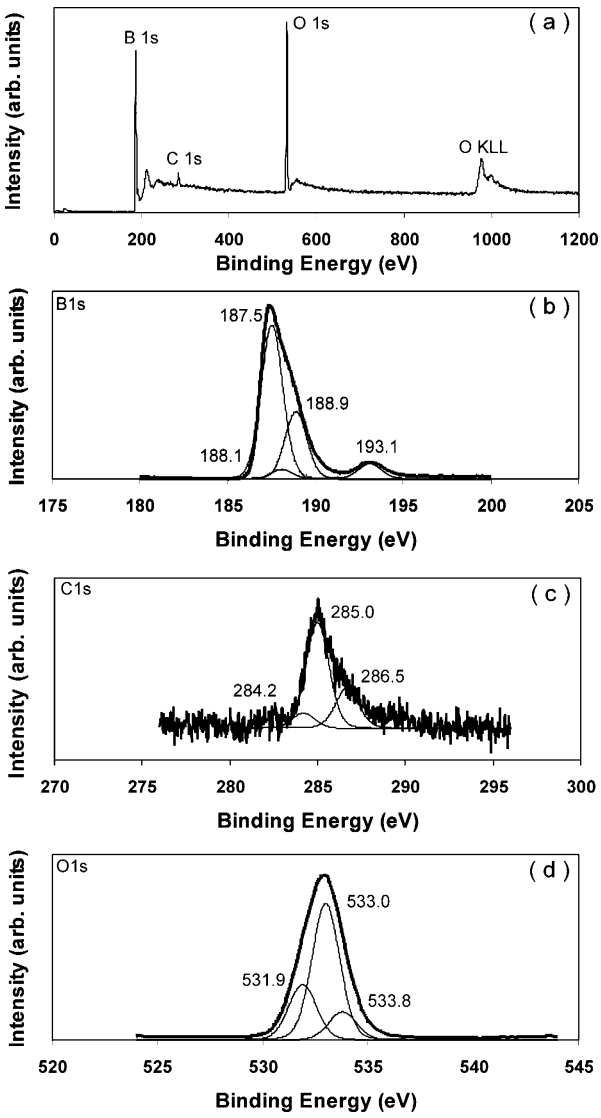

Figure 5. (a) XPS survey scan showing the B 1s, C 1s, and O 1s peak. No other element was detected in this spectrum. XPS detailed scans: (b) The B 1s peak was fit to four components at 187.5 eV, 188.1 eV, 188.9 eV and 193.1 eV, respectively; (c) the C 1s peak was fit to three components at 284.2 eV, 285.0 eV, and 286.5 eV, respectively; (d) the O 1s peak was fit to three components at 531.9 eV, 533.0 eV, and 533.8 eV, respectively. The assigned bonding types are discussed in the text.

There are several polymorphs of crystalline boron, including α-rhombohedral, β-rhombohedral, α-tetragonal, β-tetragonal, and others.[1,2] Among them, the first form to be discovered was α-tetragonal boron.[34] The unit cell originally proposed for α-tetragonal boron (B_{50}) consisted of four B_{12} icosahedra clusters, which were linked by both direct

intercluster bonds and through bonds to two isolated boron atoms.[1,34] An important feature of this unit cell is the large number of interstitial voids, which in principle could accommodate additional boron atoms as well as impurity atoms.[1] Longuet-Higgins and Roberts,[35] using quantum mechanics and the concept of closed shell boron icosahedra, pointed out that the proposed B_{50} structure would not have a stable electronic configuration and therefore could not exist. Instead, the tetragonal framework of linked icosahedra is stabilized through introduction of electron donor atoms, such as carbon, nitrogen, beryllium, or aluminum,[2,3,36] and a concentration of electron donor atoms of only 1 at. % can stabilize the structure.[2] Materials such as BeB_{12}, $AlBeB_{24}$, $B_{50}C_2$, and $B_{50}N_2$ have been assigned to the α-tetragonal boron structure.[2,3,36]

As mentioned above, the crystal structure of the boron nanoribbons reported here is α-tetragonal boron. Elemental analysis using EELS and EDX did not reveal the presence of carbon or nitrogen. However, the XPS results show a small amount of carbon, suggesting the nanoribbons might have the $B_{50}C_x$ ($0 \leq x \leq 2$) tetragonal structure. The possible source of the carbon impurity might be the gas precursor. The certificate provided by Voltaix and BOC quoted a small amount of CH_4, O_2, N_2, and CO_2 (all less than 10 ppm) in the ultrahigh purity diborane and argon we used.

Based upon the experimental results obtained from XPS analysis and TEM/EELS/EDX observation, we propose that the boron-based nanoribbon has a core of boron with a thin oxide sheath. The core is a $B_{50}C_x$ ($0 \leq x \leq 2$) tetragonal structure where B−B bonds predominate and a small amount of B−C bonds are present. The 1−2 nm thick surface layer contained mixed amorphous compounds that consist of B_2O_3, a nonstoichiometric boron-rich oxide, and a carbon−oxygen compound. This thin oxidized surface layer was most likely formed after the sample was exposed to ambient; due to the highly reducing chemical environment during synthesis, no oxide can possibly be present during synthesis.

There are several growth mechanisms for nanostructures.[37] The vapor−liquid−solid (VLS) process involves a liquid metal catalytic particle, typically located at the tip of the growing nanowire or nanotube.[38] The VLS mechanism has been invoked to explain the growth of amorphous boron nanowires using gold as a catalyst.[12] Since no catalyst was deliberately introduced for the boron nanoribbons discussed here, and no particles were observed at the ends of nanoribbons, there is no evidence of metal catalyst-assisted growth. Another mechanism for growth of semiconducting nanowires is the oxide-assisted-growth (OAG) mechanism,[39] in which an oxide layer formed on the outside of the nanowire is supposed to confine its lateral growth. The oxide layer is presumed to be molten or near molten, which might enhance atomic absorption, diffusion, and deposition. This OAG mechanism was used to interpret the growth of boron nanowires synthesized by magnetron sputtering of a target containing both B and B_2O_3.[40] As discussed above, although a small amount of oxygen was detected from our nanoribbons, we believe the oxide layer was formed by oxidation after the nanoribbons were exposed to ambient. The OAG mechanism is thus not relevant to the growth of these boron nanoribbons.

To explore the growth mechanism of the nanoribbons, a series of experiments were carried out. (1) Using the experimental parameters described above (i.e., 900 °C center position temperature, a mixture of 15 sccm diborane and 15 sccm argon gas flow, 45 min reaction time), experiments were performed on different substrates such as sapphire, fused quartz, and crystalline quartz. For each substrate, nanoribbons similar to those shown in Figure 2 were obtained, indicating the formation of the nanoribbons was substrate-independent. (2) Using Si substrates and with other parameters (i.e., center position temperature, flow rate) unchanged, the reaction time was varied from 5 to 90 min. Increasing the reaction time led to growth of more puffy balls. However, no obvious change in the morphology or dimensions of the nanoribbons was observed. In every reaction run we did, the nanoribbons were always found in the low-temperature zone region (630−750 °C, ∼1-cm long) close to the inlet of the reaction chamber. (3) Keeping the flow rate and reaction time unchanged, the reaction temperature (center position temperature) was lowered to 830 °C, 730 °C, and 630 °C, respectively. For the first case (830 °C), puffy balls were found in the 650−750 °C temperature zone region (∼ 2-cm long; the lower center temperature "spreads" the temperature gradient). For the second case (730 °C), puffy balls were found in the 650−710 °C temperature zone region (∼3 cm long). For the third case (630 °C), no puffy ball deposition was observed. SEM examination of the puffy balls, when they did grow, revealed that they consisted of nanostructures similar to those shown in Figure 2. These results confirmed that the tetragonal boron nanoribbons grow at 630−750 °C.

Considering the facts that the nanoribbons grew in the 630−750 °C region, grew in a low-pressure environment (∼200 mTorr), and have various morphologies, we believe the nanoribbon growth is largely determined by growth kinetics. The pyrolysis of diborane produces a variety of gas-phase products. Those detected by mass spectrometry include borane radicals (e.g., $^{\bullet}BH_3$, $^{\bullet}BH_2$) and other higher boranes (e.g., B_4H_{10}, B_5H_{11}, $B_{10}H_{14}$, etc.).[3] These, rather than only B_2H_6, could serve as reactants in our system. Furthermore, the deliberate use of a temperature gradient and the flow pattern in our reaction chamber might also play important roles in the formation of nanoribbons. To fully understand the growth mechanism of these tetragonal boron nanoribbons, a systematic analysis of the growth kinetics is needed.

In summary, single-crystal α-tetragonal boron nanoribbons were synthesized without catalyst by pyrolysis of diborane. The nanoribbons grew in the 630−750 °C temperature zone at 200 mTorr pressure. The growth of nanoribbons is believed to be largely determined by growth kinetics. These nanoribbons may find application in composites and as components in nanoelectromechanical systems. Also, the nanoribbon morphology may lead to product structures of various metal borides that exhibit interesting properties. For example, we may ask the question whether MgB_2 nanorib-

bons can be produced from the B nanoribbons, and if so, whether they are superconducting.

Acknowledgment. We appreciate the support of the National Science Foundation (grant EEC-0210120) and the Office of Naval Research grant (No. N000140210870). We are grateful to the NUANCE facility at Northwestern University for SEM, TEM, XPS, and FTIR measurements, and the RRC facility at the University of Illinois-Chicago for TEM and Raman spectra measurements.

Supporting Information Available: FTIR and Raman spectra of boron nanoribbons. This material is available free of charge via the Internet at http://pubs.acs.org.

References

(1) *Boron, Metallo-Boron, Compounds and Boranes*; Adams, R. M., Ed.; Interscience Publishers: New York, 1964; p 233.
(2) *Boron and Refractory Borides*; Matkovich, V. I., Ed.; Springer-Verlag: Berlin, 1977.
(3) Greenwood, N. N.; Earnshaw, A. *Chemistry of the Elements*; Reed Educational and Professional Publishing Ltd: UK, 1997; p 139.
(4) Bailey, J. E. in *Handbook of Polymer-Fibre Composites*; Jones, F. R., Eds.; Longman Scientific & Technical: Harlow, UK, 1994; p 15.
(5) Tavadze, F. N.; Lominadze, J. V.; Khvedelidze, A. F.; Tsagareishvili, G. V.; Shorshorov, M. K.; Bulichev, S. I. *J. Less-Common Met.* **1981**, *82*, 95.
(6) Boustani, I. *Phys. Rev. B* **1997**, *55*, 1.
(7) Boustani, I. *J. Solid State Chem.* **1997**, *133*, 182.
(8) Boustani, I. *Surf. Sci.* **1997**, *370*, 355.
(9) Boustani, I.; Quandt, A. *Europhys. Lett.* **1997**, *39*, 527.
(10) Boustani, I.; Quandt, A.; Hernandez, E.; Rubio, A. *J. Chem. Phys.* **1999**, *110*, 3176.
(11) Quandt, A.; Liu, A. Y.; Boustani, I. *Phys. Rev. B* **2001**, 6412.
(12) Wu, Y. Y.; Messer, B.; Yang, P. D. *Adv. Mater.* **2001**, *13*, 1487.
(13) Wu, J. Z.; Yun, S. H.; Dibos, A.; Kim, D. K.; Tidrow, M. *Microelectr. J.* **2003**, *34*, 463.
(14) Meng, X. M.; Hu, J. Q.; Jiang, Y.; Lee, C. S.; Lee, S. T. *Chem. Phys. Lett.* **2003**, *370*, 825.
(15) Cao, L. M.; Zhang, Z.; Sun, L. L.; Gao, C. X.; He, M.; Wang, Y. Q.; Li, Y. C.; Zhang, X. Y.; Li, G.; Zhang, J.; Wang, W. K. *Adv. Mater.* **2001**, *13*, 1701.
(16) Cao, L. M.; Hahn, K.; Wang, Y. Q.; Scheu, C.; Zhang, Z.; Gao, C. X.; Li, Y. C.; Zhang, X. Y.; Sun, L. L.; Wang, W. K.; Ruhle, M. *Adv. Mater.* **2002**, *14*, 1294.
(17) Zhang, Y. J.; Ago, H.; Yumura, M.; Komatsu, T.; Ohshima, S.; Uchida, K.; Iijima, S. *Chem. Commun.* **2002**, 2806.
(18) Otten, C. J.; Lourie, O. R.; Yu, M. F.; Cowley, J. M.; Dyer, M. J.; Ruoff, R. S.; Buhro, W. E. *J. Am. Chem. Soc.* **2002**, *124*, 4564.
(19) Wang, Y. Q.; Duan, X. F. *Appl. Phys. Lett.* **2003**, *82*, 272.
(20) Yang, Q.; Sha, J.; Xu, J.; Ji, Y. J.; Ma, X. Y.; Niu, J. J.; Hua, H. Q.; Yang, D. R. *Chem. Phys. Lett.* **2003**, *379*, 87.
(21) Wang, Z. K.; Shimizu, Y.; Sasaki, T.; Kawaguchi, K.; Kimura, K.; Koshizaki, N. *Chem. Phys. Lett.* **2003**, *368*, 663.
(22) Komatsu, S.; Moriyoshi, Y. *J. Cryst. Growth* **1990**, *102*, 899.
(23) JCPDS-International Centre for Diffraction Data, PCPDFWIN, v. 2.4, 2003.
(24) Budd, P. M.; Goodhew, P. J. *Light-Element Analysis in the Transmission Electron Microscope: WEDX and EELS*; Oxford Science Publications: UK, 1988; p 59.
(25) Quantitative analysis was performed using Gatan EELS Analysis package within DigitalMicrograph image acquisition and processing software.
(26) Cooper, H. In *Rare Metals Handbook*; Hampel, C. A., Eds.; Reinhold Publishing Corporation: London, 1954; p 71.
(27) Ronning, C.; Schwen, D.; Eyhusen, S.; Vetter, U.; Hofsass, H. *Surf. Coat. Technol.* **2002**, *158*, 382.
(28) *Handbook of X-ray Photoelectron Spectroscopy*; Moulder, J., Stickle, W., Sobel, P., Bomben, E., Eds.; Physical Electronics: Eden Prairie, 1995.
(29) Ennaceur, M. M.; Terreault, B. *J. Nucl. Mater.* **2000**, *280*, 33.
(30) Belyansky, M.; Trenary, M. *Surf. Sci. Spectra* **1995**, *3*, 147.
(31) Wang, Y.; Trenary, M. *Chem. Mater.* **1993**, *5*, 199.
(32) *CRC Handbook of Chemistry and Physics (electronic source)*, 84th ed.; CRC press: Boca Raton, FL, 2003−2004.
(33) *Surface Analysis−The Principle Techniques*; Vickerman, J. C., Ed.; John Wiley & Sons: Chichester, England, 1997.
(34) Laubengayer, A. W.; Hurd, D. T.; Newkirk, A. E.; Hoard, J. L. *J. Am. Chem. Soc.* **1943**, *64*, 1924.
(35) Longuet-Higgins, H. C.; Roberts, M. d. V. *Proc. R. Soc. A* **1955**, *230*, 110.
(36) Will, G.; Ploog, K. *Nature* **1974**, *251*, 406.
(37) Xia, Y. N.; Yang, P. D.; Sun, Y. G.; Wu, Y. Y.; Mayers, B.; Gates, B.; Yin, Y. D.; Kim, F.; Yan, Y. Q. *Adv. Mater.* **2003**, *15*, 353.
(38) Wagner, R. S.; Ellis, W. C. *T. Metall. Soc. AIME* **1965**, *233*, 1053.
(39) Zhang, R. Q.; Lifshitz, Y.; Lee, S. T. *Adv. Mater.* **2003**, *15*, 635.
(40) Wang, Y. Q.; Duan, X. F.; Cao, L. M.; Wang, W. K. *Chem. Phys. Lett.* **2003**, *369*, 704.

NL0498785